Domain-wall dynamics in Bose-Einstein condensates with synthetic gauge fields

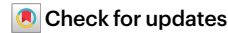
https://doi.org/10.1038/s41586-021-04250-3

Kai-Xuan Yao^{1,2,3}, Zhendong Zhang^{1,2,3} & Cheng Chin^{1,2,3} ⊠

Received: 11 June 2021

Accepted: 16 November 2021

Published online: 2 February 2022



Interactions in many-body physical systems, from condensed matter to high-energy physics, lead to the emergence of exotic particles. Examples are mesons in quantum chromodynamics and composite fermions in fractional quantum Hall systems, which arise from the dynamical coupling between matter and gauge fields^{1,2}. The challenge of understanding the complexity of matter-gauge interaction can be aided by quantum simulations, for which ultracold atoms offer a versatile platform via the creation of artificial gauge fields. An important step towards simulating the physics of exotic emergent particles is the synthesis of artificial gauge fields whose state depends dynamically on the presence of matter. Here we demonstrate deterministic formation of domain walls in a stable Bose–Einstein condensate with a gauge field that is determined by the atomic density. The density-dependent gauge field is created by simultaneous modulations of an optical lattice potential and interatomic interactions, and results in domains of atoms condensed into two different momenta. Modelling the domain walls as elementary excitations, we find that the domain walls respond to synthetic electric field with a charge-to-mass ratio larger than and opposite to that of the bare atoms. Our work offers promising prospects to simulate the dynamics and interactions of previously undescribed excitations in quantum systems with dynamical gauge fields.

Gauge theories form a cornerstone in our understanding of condensed-matter systems³ and fundamental particles⁴. A complete theoretical understanding of many-body systems subject to gauge fields, however, faces major analytical and numerical challenges^{5,6}. Experiments with ultracold atoms offer an alternative approach by quantum simulating gauge theory models, where gauge fields can be artificially synthesized⁷⁻⁹. Much progress has been made in the past few years on creating static artificial gauge fields in atomic quantum gases¹⁰, enabling the realization of, for instance, the iconic Haldane¹¹ and Hofstadter models^{12,13}.

Fundamentally, gauge fields are dynamical, with quantum degrees of freedom that interact with matter^{14–18}. An intriguing consequence of the dynamical feedback between the matter and the gauge field is the formation of previously undescribed particle-like excitations with emergent properties, for example, mesons in the standard model¹ and composite fermions in the fractional quantum Hall effect². Recently, several experiment groups have realized density-dependent gauge fields¹⁹⁻²¹, where the strength of the field depends on the density of matter²², as well as lattice gauge theory models²³⁻²⁵.

In this work, we quantum simulate a Bose–Einstein condensate (BEC) subject to a density-dependent gauge field, which is described by the energy density functional

$$\mathcal{H} = \frac{1}{2m^*} \left| (\mathbf{p} - \mathcal{A})\psi \right|^2 + \frac{1}{2}g \left| \psi \right|^4, \tag{1}$$

where ψ is the condensate wavefunction, \mathbf{p} is the momentum operator, m^* is the mass of the particle, A is the density-dependent gauge field and g is the interaction strength. We engineer a gauge field that takes one of two values according to the density $n = |\psi|^2$,

$$A = \hbar k^* \operatorname{sign}(n - n_c)\hat{x}, \tag{2}$$

where $k^* > 0$ is a constant, sign(x) = x/|x| is the sign function and \hbar is the reduced Planck constant. The gauge field is along the $+\hat{x}$ direction when the density exceeds the critical value n_c and along $-\hat{x}$ at lower densities (see Fig. 1). We observe the formation of stable domain walls in the BEC. which are topological defects²⁶, and extract an effective charge-to-mass ratio from their dynamical response to the gauge field.

In the BEC described by equation (1), the local phase gradient of the ground-state wavefunction follows the gauge field, $\partial_x \phi = k^* \operatorname{sign}(n - n_c)$, to minimize the kinetic energy. The condensate can support two types of domains with momentum $k = +k^*$ for density n exceeding the critical value n_c and momentum $k = -k^*$ for lower density $n < n_c$. The density-dependent magnetic field $\mathbf{B} = \nabla \times \mathcal{A} = -2\hbar k^* \delta(n - n_c) \partial_{\nu} n\hat{z}$ is concentrated on domain walls parallel to the gauge field, and $\delta(x)$ is the Dirac delta function. On the other hand, dynamics of the density generates an electric field $\mathbf{E} = -\partial_t A = -2\hbar k^* \delta(n - n_c) \partial_t n\hat{x}$. The electro $magnetic fields \, \boldsymbol{E} \, and \, \boldsymbol{B} \, can \, induce \, Lorentz \, force \, on \, the \, atoms, simulations \, and \, \boldsymbol{E} \, can \, induce \, \boldsymbol{E} \, can \, \boldsymbol{E} \, \boldsymbol{E} \, can \, \boldsymbol{E} \,$ ing charged particles in the gauge field.

In our experiment, we load a nearly pure BEC of around 40,000 ^{133}Cs atoms into a 1D optical lattice along the x direction, with an additional direction of the xtional weak harmonic confinement in the x-y plane at the radial trap frequency $2\pi \times 8$ Hz and a tight vertical confinement at the trap frequency $2\pi \times 223$ Hz. The condensate remains in the 3D regime, with a

¹James Franck Institute, University of Chicago, Chicago, IL, USA. ²Enrico Fermi Institute, University of Chicago, Chicago, IL, USA. ³Department of Physics, University of Chicago, Chicago, IL, USA. [™]e-mail: cchin@uchicago.edu

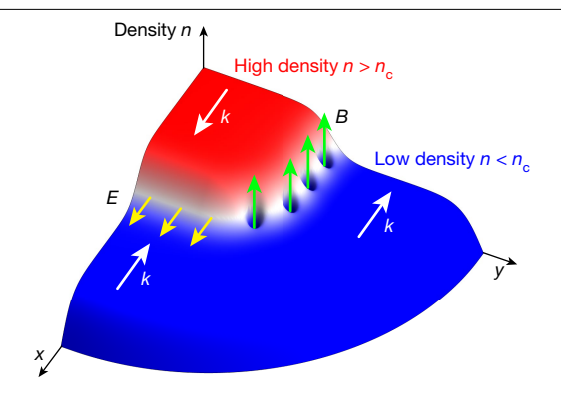


Fig. 1| **Illustration of a Bose–Einstein condensate with a density-dependent gauge field.** A condensate with inhomogeneous density profile is subject to a density-dependent gauge field \mathcal{A} , which changes sign when the density n exceeds a critical value n_c . The high-density (red) and low-density (blue) regions of the condensate form domains with distinct momenta $k = k^*$ and $-k^*$ in the x direction (white arrows), respectively. Along the domain wall (white) parallel to the gauge field, an array of vortices form as a consequence of phase continuity, which is a manifestation of the effective magnetic field $B \approx \partial_y n$ (green arrows). On the other hand, dynamics of the condensate density can induce an effective electric field $E \approx \partial_t n$ (yellow arrows). In this work, we observe the formation and dynamics of domain walls perpendicular to the gauge field.

chemical potential $2\pi \times 170$ Hz. Using Floquet engineering²⁷, we realize the gauge field in equation (2) by generating a tilted double-well dispersion ϵ_k along the lattice direction, where the energy offset of the two wells depends on the density of the sample. The dispersion can be modelled by

$$\epsilon_k = \alpha \left(k^2 - k^{*2}\right)^2 - \frac{\hbar}{m^*} kA(n). \tag{3}$$

Here k is the wavenumber, α and k^* can be controlled by lattice shaking along the x direction, m^* is the effective mass near $k = \pm k^*$ and the gauge field $A = A_s + A_d(n)$ contains the static and density-dependent contributions A_s and $A_d(n)$, respectively, which we generate from synchronous modulations of the lattice potential and the interatomic interaction, respectively. See Fig. 2). The presence of the gauge field A shifts the local minima of the dispersion to $k = \pm k^* + A$ to leading order.

We modulate the lattice position δx in time t at two frequencies according to $\delta x(t) = X_1 \sin \omega t + X_2 \sin 2\omega t$ (see Fig. 2a), where the modulation amplitude X_1 determines α and k^* of the double-well dispersion, and the amplitude X_2 imbalances the two minima²⁸. The fundamental frequency ω is red detuned to the second excited band of the lattice at zero momentum (see Fig. 2b and Methods). The shaking induces a direct single-photon coupling at frequency ω and coupling strength Ω_1 , as well as a Raman coupling involving both an ω photon and a 2ω photon with coupling strength Ω_2 . The direct coupling Ω_1 has an odd parity that only mixes states with non-zero momentum $k \neq 0$, essential for the creation of the double-well dispersion (see Fig. 2c). On the other hand, the Raman coupling Ω_2 has an even parity. The interference of the two couplings Ω_1 and Ω_2 with opposite parities results in the imbalance of the two dispersion minima. We control the imbalance in our experiment with the amplitude of the second harmonic modulation X_2 , which results in a static gauge field $A_s \propto -X_2$. See Methods for details.

The static gauge field A_s manifests in the momentum distribution of the BEC. Based on the focused time-of-flight method²⁹, we see that the condensate momentum indeed takes on values $k = \pm k^*$, depending on the sign of X_2 (see Fig. 2d). For the remainder of this work, we choose $X_2 = 23$ nm, which imbalances the two wells by $h \times 3$ Hz.

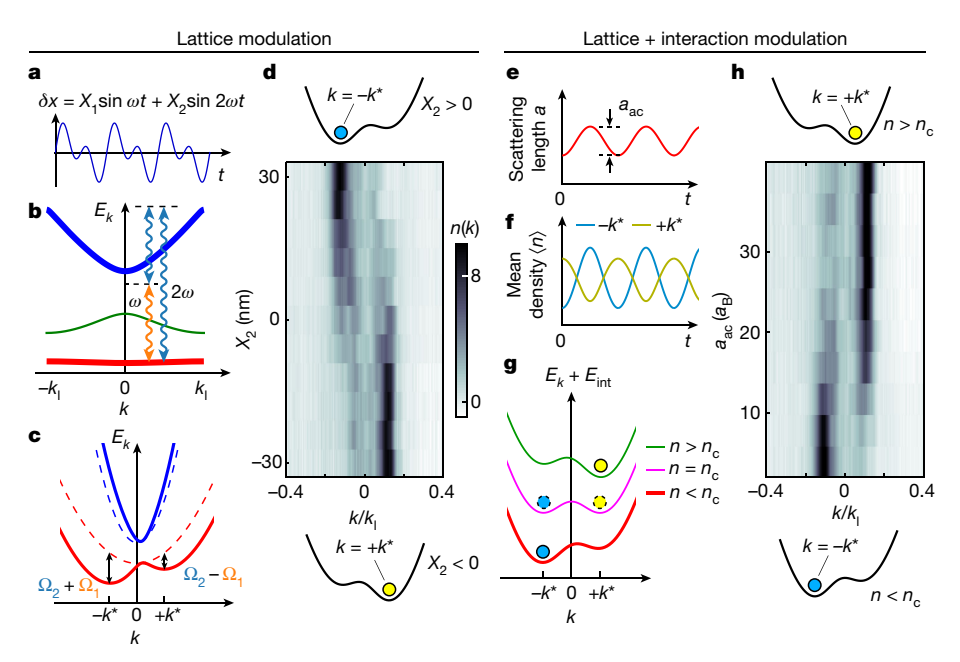


Fig. 2 | **Creation of static and density-dependent gauge fields.** Static gauge fields are shown in panels **a**–**d** and density-dependent gauge fields are shown in panels **e**–**h**. **a**, We periodically translate the 1D optical lattice by $\delta x = X_1 \sin \omega t + X_2 \sin 2\omega t$ with $X_1 = 21$ nm and variable X_2 . **b**, The frequency ω is slightly red detuned from the transition between the ground band (red) and the second excited band (blue). The first excited band (green) is only weakly coupled. Here $k_1 = \pi/(532 \text{ nm})$. The shaking introduces a direct coupling Ω_1 (orange arrow) and a Raman coupling Ω_2 (blue arrows). **c**, In the Floquet picture, the two couplings destructively (constructively) interfere for positive (negative) k when k₂ > 0. The couplings hybridize the bare bands (dashed lines) and the resulting ground band (red line) forms a tilted double well with minima

at $k \approx \pm k^* = \pm 0.15k_1$. **d**, Time-of-flight images show a jump of the BEC momentum when X_2 flips sign. See illustrations for the dispersions with $X_2 > 0$ and $X_2 < 0$. The 1D momentum distribution n(k) is normalized over the first Brillouin zone. **e**, The scattering length a is modulated at frequency ω . **f**, The micromotion of the atomic density $\langle n \rangle$ at $k = \mp k^*$ oscillates in and out of phase with the scattering-length modulation. This results in a higher interaction energy for $k = -k^*$ than for $k = +k^*$. **g**, Combining both modulations yields a dispersion whose minimum position depends on the density as $k = k^*$ sign $(n - n_c)$. **h**, The momentum distribution of the BEC shows a jump when a_{ac} exceeds 14(2) a_B . See illustrations for the dispersions with $n > n_c$ and $n < n_c$.

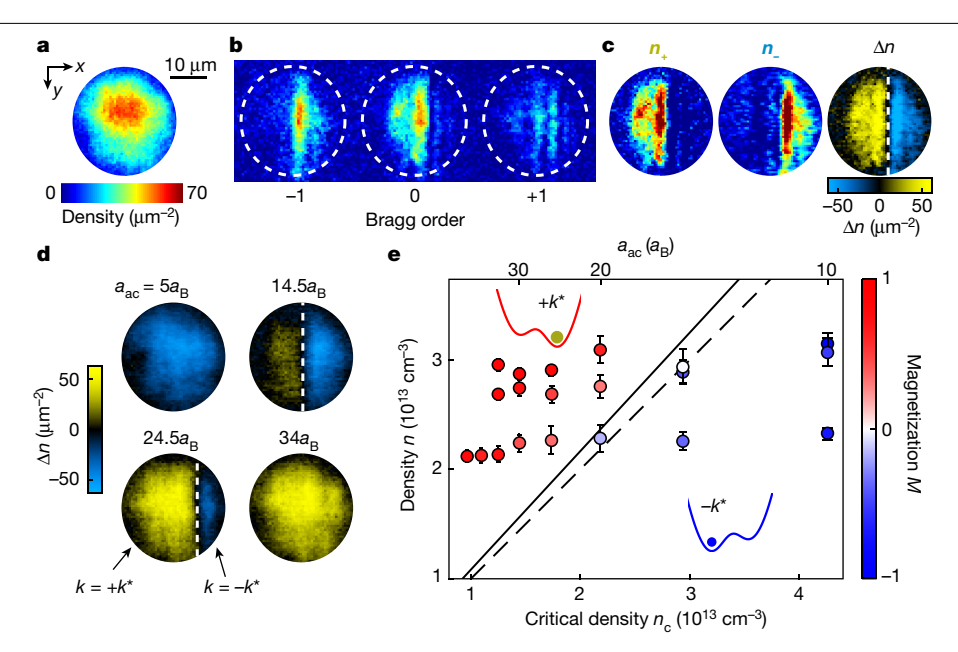


Fig. 3 | Domains and domain walls in the presence of a density-dependent gauge field. a, In situ image of the BEC in a harmonic trap shows a non-uniform density profile. The scale bar applies to all images in panels a-d.b, The BEC is Bragg diffracted by the lattice after a 6-ms time-of-flight expansion. Atomic populations in $k = \pm k^*$ states are transferred to different Bragg orders. Here a single-shot image is shown, c. From the image, we reconstruct the density profiles $n_{+}(\mathbf{r})$ of the $\pm k^{*}$ domains. The difference $\Delta n = n_{+} - n_{-}$ reveals the domain structure and $\Delta n = 0$ indicates the domain wall (white dashed line). **d**, Examples

of the domain structure are shown at various modulation amplitudes a_{ac} . Each image is an average over 15 realizations, e. The magnetization M near the centre of the cloud is compared for different critical density n_c and atomic density n. The dotted line indicates the predicted location for M = 0, with $n = n_c = \epsilon/g_{ac}$ and $\epsilon = h \times 21.5$ Hz. The experimental fit (solid line) yields $\epsilon_{\rm exp} = h \times 23(1)$ Hz. See Methods for details. Each data point is an average of 15 samples. Error bars denote one standard deviation.

The density-dependent part of the gauge field A_d is created by modulating the scattering length a with an external magnetic field19 at the same fundamental frequency as the lattice shaking $a(t) = a_{dc} - \frac{1}{2}a_{ac}\cos\omega t$ (see Fig. 2e), where $a_{dc} = 50a_{B}$ and a_{ac} are the mean scattering length and the amplitude of the modulation, respectively, and $a_{\rm B}$ is the Bohr radius. To understand the density dependence of the gauge field, we note that the atoms in the $k = \pm k^*$ states acquire a time-dependent micromotion from the lattice shaking. Within a Floquet cycle, the atomic density of the two states $k = \pm k^*$ oscillates at frequency ω with opposite phase ¹⁹ (see Fig. 2f). We modulate the scattering length in phase with the atomic density in the state $k = -k^*$, which raises the time-averaged interaction energy for $k = -k^*$ and lowers that for $k = +k^*$. This results in a coupling between the density and the momentum, favouring the $k = +k^*$ state. The coupling gives the densitydependent part of the gauge field $A_d = \eta g_{ac} n$, where $g_{ac} = 4\pi \hbar^2 a_{ac}/m_0$ is the AC coupling constant, m_0 is the mass of the caesium atom and η can be calculated from the micromotion (see Methods).

Combining the lattice and interaction modulations, we can write the resulting gauge field as

$$A = A_{s} + A_{d}(n) = \eta g_{ac}(n - n_{c}),$$
 (4)

where the critical density n_c , at which the gauge field switches sign, is given by

$$n_{\rm c} = \epsilon / g_{\rm ac} \tag{5}$$

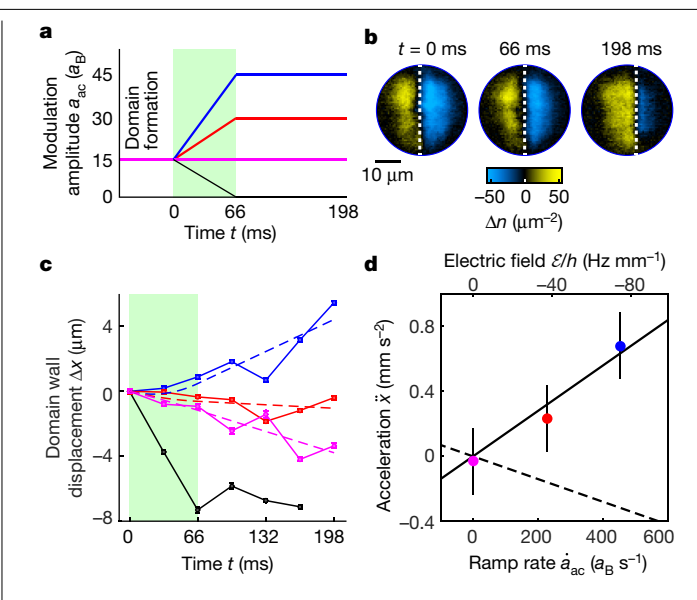
and $\epsilon = -A_s/\eta$. When the atomic density exceeds the critical density n_c , the dispersion minimum switches from $k = -k^*$ to $+k^*$. For a BEC residing at the lowest energy state, its momentum also changes sign when the density exceeds the critical value (see Fig. 2g). Therefore the BEC can be effectively described by the energy functional equation (1) with the gauge field A in equation (2), which has a step-function dependence on the density.

To demonstrate the effect of the density-dependent gauge field, we measure the condensate momentum in the presence of both lattice and interaction modulations. We find that the condensate momentum indeed changes sign from $k = -k^*$ to $+k^*$ at $a_{ac} = 14(2)a_B$, where the critical density n_c is comparable with the density of the sample (see Fig. 2h). Our observation is consistent with the dispersion ϵ_k in equation (3) with the density-dependent gauge field A(n) in equation (4).

In a trapped gas, where the condensate has non-uniform density (see Fig. 3a), we expect the condensate momentum to develop spatial structures in the presence of the density-dependent gauge field. In the following, we investigate the formation and dynamics of domains with different momentum in the condensate.

Starting with a regular BEC in a stationary 1D lattice, we slowly ramp up the lattice and interaction modulations over 300 ms. At the end of the ramp, the dispersion has two minima at $k = \pm k^*$, around which the effective mass is $m^* = 0.7m_0$. The BEC has a 1/e lifetime of 700 ms under the driving. We measure the spatial distribution $n_{+}(\mathbf{r})$ of the atoms in the $k = \pm k^*$ states by first transferring the population in the two states to different Brillouin zones, followed by a short time of flight, which maps the population to different Bragg orders³⁰ (see Fig. 3b, c and Methods). Domain structures of the condensate are revealed by the density difference $\Delta n(\mathbf{r}) = n_{+}(\mathbf{r}) - n_{-}(\mathbf{r})$.

For moderate interaction modulation amplitudes $14a_B < a_{ac} < 25a_B$, we observe regions of atoms in the same momentum state separated by a domain wall in over 90% of the samples (see Fig. 3d). The separation of domains results from effective ferromagnetic interactions between the $+k^*$ and $-k^*$ states³¹. The domain wall forms perpendicular to the lattice direction. We do not observe parallel domain walls with the predicted vortex arrays, probably because of their higher energy cost under our conditions. In addition, we see that the left (right) side of the condensate tends to occupy rightward (leftward) momentum (see Fig. 3d), which we attribute to the shrinkage of the cloud during the ramp that preferentially pulls atoms towards the centre. See Methods for details. The position of the domain wall depends on the density



 $Fig.\,4\,|\,Dynamics\,of\,the\,domain\,wall\,in\,response\,to\,a\,synthetic\,electric\,field$ \mathcal{E} . a, After forming the domains at modulation strength $a_{ac} = 15a_{B}$, we ramp to $a_{ac} = 0a_B$ (black), $15a_B$ (magenta), $30a_B$ (red) or $45a_B$ (blue) over 66 ms and hold for 132 ms. The ramp induces an electric field $\mathcal{E} \propto \dot{a}_{ac}$ (green shaded area). **b**, Example images for the ramp to $a_{ac} = 45a_B$. The white dashed lines mark the positions of the domain walls. Each image is the average of 15 samples. c, The domain-wall dynamics: dashed lines are fits based on equation (8). The black data points are excluded from the fit because the domain wall moves out of the cloud. \mathbf{d} , The acceleration \ddot{x} extracted from the fit shows a linear dependence on the ramp rate \dot{a}_{ac} and the electric field \mathcal{E} . The linear fit $\ddot{x} = \beta \dot{a}_{ac}$ (black line) gives $\beta = -26(6) \text{ ms}^{-1}$. The prediction for bare atoms gives $\beta_{\text{atom}} = 13 \text{ ms}^{-1}$ (dashed line). Error bars indicate one standard deviation.

and the interaction modulation amplitude a_{ac} , providing a test of the strength of the density-dependent gauge field.

We analyse the momentum distribution in the condensate through the local magnetization defined as

$$M(\mathbf{r}) = \frac{n_{+}(\mathbf{r}) - n_{-}(\mathbf{r})}{n_{+}(\mathbf{r}) + n_{-}(\mathbf{r})}.$$
 (6)

A value of M = +1 indicates that all atoms condense in the $+k^*$ state. M = -1 indicates the condensate in the $-k^*$ state and M = 0 indicates a domain wall.

We perform the experiment with different atom numbers and modulation amplitudes a_{ac} . We extract the magnetization M near the centre of the condensate for various atomic density $n = n_+ + n_-$ and critical density $n_c = \epsilon/g_{ac}$ (see Fig. 3e). We find that the local momentum indeed settles to $+k^*$ for densities exceeding n_c and to $-k^*$ for $n < n_c$. From the experimental data, we also extract the coefficient ϵ and the result $\epsilon_{\rm exp} = h \times 23(1)$ Hz is in good agreement with the prediction $\epsilon = h \times 21.5$ Hz.

The deterministic formation of domains offers an opportunity to study the domain walls as elementary objects, which is of fundamental interest to condensed-matter physics³², high-energy physics³³ and cosmology³⁴. We introduce a phenomenological model that describes the domain wall as an elementary excitation with charge Q and mass M^* interacting with the same gauge field A experienced by the underlying atoms, with energy

$$E = \sigma \Lambda + \frac{(\mathbf{P} - Q\mathbf{A})^2}{2M^*},\tag{7}$$

where $\mathbf{P} = M^*\mathbf{v} + Q\mathbf{A}$ and \mathbf{v} are the canonical momentum and velocity of the domain wall, respectively, A is the area of the domain wall, the surface tension $\sigma = \frac{8}{3} \varepsilon n/k^*$ is calculated in ref. ²⁶ and ε is the barrier height of the double-well dispersion. For our parameters, $\varepsilon = h \times 4$ Hz and the rest energy of the domain wall $\sigma \Lambda \approx k_{\rm B} \times 1$ nK per atom in the domain wall.

For our observed domain walls perpendicular to the lattice along the x axis, their motion is restricted to the same direction. The dynamics is driven by the Lorentz force with only the electric field in the x direction $\mathcal{E} = -\partial_t A$, with A given in equation (4). We derive

$$\ddot{x} = \frac{Q}{M^*} \mathcal{E}$$

$$\mathcal{E} = -\frac{\partial \eta(g_{ac} n - \epsilon)}{\partial t}.$$
(8)

To study the dynamical response of the domain wall to the electric field \mathcal{E} , we ramp the density-dependent gauge field and monitor the motion of the domain wall. After preparing one domain wall in the BEC at the modulation strength $a_{ac} = 15a_{B}$, we ramp a_{ac} to different values over 66 ms, which induces an electric field \mathcal{E} . We then hold for another 132 ms, during which the domain wall can freely propagate (see Fig. 4a).

We observe that the domain wall moves in the lattice direction in response to the ramp (see Fig. 4b, c), consistent with the direction of the electric field. The motion persists in the same direction after the ramp stops. From equation (8), we expect that the domain wall accelerates during the ramp $\ddot{x} = \beta \dot{a}_{ac}$, where $\beta \propto Q/M^*$, and maintains a constant velocity during the hold time. (The atomic density *n* remains almost constant to within 20% during the dynamics, and η and ϵ are constants.) We fit the domain-wall trajectories to extract the acceleration \ddot{x} , which indeed shows a linear dependence on the ramp rate \dot{a}_{ac} (see Fig. 4d). From the linear fit, we extract the charge-to-mass ratio of the domain wall to be $Q/M^* = -2.8(7) m_0^{-1}$, where m_0 is the mass of a caesium atom.

Our measurements present an interesting result where the topological defect in the BEC with a density-dependent gauge field behaves very differently from the bare atoms. A bare atom residing near a local minimum of the double-well dispersion described in equation (3) also accelerates under the electric field \mathcal{E} because the gauge field A shifts the minima to $k = \pm k^* + A$. To leading order in the electric field \mathcal{E} , the charge-to-mass ratio of an atom is $1/m^* = 1.4 m_0^{-1}$. This suggests that the electric field propels the domain wall in the opposite direction compared with the bare atoms at 2.0(5) times the acceleration. Notably, the direction of domain-wall motion is consistent with the condensate relaxing to the momentum state with lower energy. A quantitative understanding of the different responses between the domain wall and the bare atoms demands further theoretical and experimental investigation.

In summary, we demonstrate deterministic creation of domain walls in a BEC with a density-dependent gauge field, created by simultaneous modulations of the lattice potential and the interaction strength. The domain walls remain stable in the BEC and behave like elementary excitations. Their dynamical response to the gauge field is observed to be drastically different from the bare atoms. Our work offers promising prospects of Floquet engineering of optical lattices and atomic interactions as a powerful tool to simulate the dynamics and interactions of topological defects such as domain walls and vortex lines. Synthesis of dynamical gauge fields that respect local gauge symmetry can also be realized with Floquet engineering of spin-dependent optical lattices³⁵.

Online content

Any methods, additional references, Nature Research reporting summaries, source data, extended data, supplementary information, acknowledgements, peer review information; details of author contributions and competing interests; and statements of data and code availability are available at https://doi.org/10.1038/s41586-021-04250-3.

Article

- Griffiths, D. Introduction to Elementary Particles (Wiley, 2008).
- Stormer, H. L., Tsui, D. C. & Gossard, A. C. The fractional quantum Hall effect. Rev. Mod. 2 Phys. 71, S298-S305 (1999).
- 3. Kogut, J. B. An introduction to lattice gauge theory and spin systems. Rev. Mod. Phys. 51, 659-713 (1979).
- Wilson, K. G. Confinement of quarks. Phys. Rev. D 10, 2445-2459 (1974).
- Alford, M. G., Schmitt, A., Rajagopal, K. & Schäfer, T. Color superconductivity in dense quark matter. Rev. Mod. Phys. 80, 1455-1515 (2008).
- 6. Troyer, M. & Wiese, U.-J. Computational complexity and fundamental limitations to fermionic quantum Monte Carlo simulations. Phys. Rev. Lett. 94, 170201 (2005).
- 7. Goldman, N., Juzeliūnas, G., Öhberg, P. & Spielman, I. B. Light-induced gauge fields for ultracold atoms. Rep. Prog. Phys. 77, 126401 (2014).
- 8. Zohar, E., Cirac, J. I. & Reznik, B. Quantum simulations of lattice gauge theories using ultracold atoms in optical lattices, Rep. Prog. Phys. 79, 014401 (2015).
- 9. Cooper, N. R., Dalibard, J. & Spielman, I. B. Topological bands for ultracold atoms. Rev. Mod. Phys. 91, 015005 (2019).
- 10. Lin, Y., Compton, R., Jiménez-García, K., Porto, J. V. & Spielman, I. B. Synthetic magnetic fields for ultracold neutral atoms, Nature 462, 628-632 (2009).
- Jotzu, G. et al. Experimental realization of the topological Haldane model with ultracold 11. fermions, Nature 515, 237-240 (2014).
- 12 Aidelsburger, M. et al. Realization of the Hofstadter Hamiltonian with ultracold atoms in optical lattices. Phys. Rev. Lett. 111, 185301 (2013).
- $\label{eq:miyake} \mbox{Miyake, H., Siviloglou, G. A., Kennedy, C. J., Burton, W. C. \& Ketterle, W. Realizing the}$ 13. Harper Hamiltonian with laser-assisted tunneling in optical lattices. Phys. Rev. Lett. 111, 185302 (2013)
- Baskaran, G. & Anderson, P. W. Gauge theory of high-temperature superconductors and strongly correlated Fermi systems. Phys. Rev. B 37, 580-583 (1988).
- Cheng, T.-P. & Li, L.-F. Gauge Theory of Elementary Particle Physics (Oxford Univ. Press, 1994).
- Levin, M. & Wen, X.-G. Colloquium: photons and electrons as emergent phenomena. Rev. Mod. Phys. 77, 871-879 (2005).
- Wiese, U.-J. Ultracold quantum gases and lattice systems: quantum simulation of lattice gauge theories. Ann. Phys. 525, 777-796 (2013).
- 18. Savary, L. & Balents, L. Quantum spin liquids: a review. Rep. Prog. Phys. 80, 016502
- Clark, L. W. et al. Observation of density-dependent gauge fields in a Bose-Einstein condensate based on micromotion control in a shaken two-dimensional lattice. Phys. Rev. Lett. 121, 030402 (2018).

- Görg, F. et al. Realization of density-dependent Peierls phases to engineer quantized gauge fields coupled to ultracold matter. Nat. Phys. 15, 1161-1167 (2019)
- Lienhard, V. et al. Realization of a density-dependent Peierls phase in a synthetic, spin-orbit coupled Rydberg system. Phys. Rev. X 10, 021031 (2020).
- Edmonds, M. J., Valiente, M., Juzeliūnas, G., Santos, L. & Öhberg, P. Simulating an interacting gauge theory with ultracold Bose gases. Phys. Rev. Lett. 110, 085301
- 23. Schweizer, C. et al. Floquet approach to \mathbb{Z}_2 lattice gauge theories with ultracold atoms in optical lattices. Nat. Phys. 15, 1168-1173 (2019).
- Yang, B. et al. Observation of gauge invariance in a 71-site Bose-Hubbard quantum simulator. Nature 587, 392-396 (2020).
- Mil, A. et al. A scalable realization of local U(1) gauge invariance in cold atomic mixtures. Science 367, 1128-1130 (2020).
- 26. Liu, T., Clark, L. W. & Chin, C. Exotic domain walls in Bose-Einstein condensates with double-well dispersion, Phys. Rev. A 94, 063646 (2016)
- 27. Eckardt, A. Colloquium: atomic quantum gases in periodically driven optical lattices. Rev. Mod. Phys. 89, 011004 (2017).
- 28. Struck, J. et al. Tunable gauge potential for neutral and spinless particles in driven optical lattices, Phys. Rev. Lett. 108, 225304 (2012).
- 29. Shvarchuck, I. et al. Bose-Einstein condensation into nonequilibrium states studied by condensate focusing. Phys. Rev. Lett. 89, 270404 (2002).
- Clark, L. W., Feng, L. & Chin, C. Universal space-time scaling symmetry in the dynamics of bosons across a quantum phase transition. Science 354, 606-610 (2016).
- Parker, C. V., Ha, L.-C. & Chin, C. Direct observation of effective ferromagnetic domains of cold atoms in a shaken optical lattice. Nat. Phys. 9, 769-774 (2013).
- Mermin, N. D. The topological theory of defects in ordered media. Rev. Mod. Phys. 51, 32. 591-648 (1979).
- Gani, V. A., Kudryavtsev, A. E. & Lizunova, M. A. Kink interactions in the (1+1)-dimensional φ⁶ model. Phys. Rev. D **89**, 125009 (2014).
- Vilenkin, A. Cosmic strings and domain walls. Phys. Rep. 121, 263-315 (1985).
- Barbiero, L. et al. Coupling ultracold matter to dynamical gauge fields in optical lattices: from flux attachment to \mathbb{Z}_2 lattice gauge theories. Sci. Adv. **5**, eaav7444 (2019).

Publisher's note Springer Nature remains neutral with regard to jurisdictional claims in published maps and institutional affiliations.

© The Author(s), under exclusive licence to Springer Nature Limited 2022

Methods

Floquet engineering of the gauge fields A_s and A_d

An atom in our shaken optical lattice evolves according to the following Hamiltonian,

$$H = \frac{p^2}{2m} + \frac{U}{2} \cos k_0 (x - \delta x),$$

where p is the 3D momentum of the atom, U is the lattice depth, k_0 is the lattice wavenumber and $\delta x = X_1 \sin \omega t + X_2 \sin 2\omega t$ is the lattice displacement. On the single-particle level, the dynamics in the y and z directions are decoupled and we focus on the x direction. The time-dependent Hamiltonian has discrete translational symmetry of the lattice and the Hamiltonian separates for different quasi-momentum quantum numbers k as $H = \bigotimes_k H(k)$. We numerically calculate the dispersion of the Floquet bands by diagonalizing the Floquet operator $U_F(k) = e^{-i\int_0^T H(k) \mathrm{d}t}$ in momentum space, including the first 15 bands in the Hilbert space, and Trotterizing the time evolution into 100 steps. The operator is diagonalized as $U_F(k) = \sum_j e^{-i\epsilon_j(k)T/\hbar} |\psi_j(k)\rangle \langle \psi_j(k)|$. The

The operator is diagonalized as $U_F(k) = \sum_j \mathrm{e}^{-\mathrm{i} \varepsilon_j(k)T/\hbar} |\psi_j(k)\rangle \langle \psi_j(k)|$. The eigenvalues $\varepsilon_j(k)$ are the quasi-energies, giving the effective dispersion of the hybridized bands. The eigenvectors contain the micromotion of the Floquet eigenstates $|\Psi_j(k,t)\rangle = \mathrm{e}^{-\mathrm{i}\int_0^T H(k)\mathrm{d}\tau} |\psi_j(k)\rangle$, from which we calculate the micromotion of the density $\langle n(t)\rangle = \int |\Psi_j(x,t)|^4 \mathrm{d}x$ shown in Fig. 2f.

The scattering length is modulated as $a(t) = a_{\rm dc} - \frac{1}{2} a_{\rm ac} \cos \omega t$. The time-averaged interaction energy (chemical potential) is $E_{\rm int} = \frac{N}{V} \frac{1}{T} \frac{4\pi\hbar^2}{m_0} \int \langle n(t) \rangle a(t) dt$, for N atoms in volume V, corresponding to experimentally measured atomic density N/V, which is averaged over length scales large than the lattice constant.

Comparing the interaction energy $E_{\rm int}$ for $k=\pm k^*$ states, we obtain the factor η in the expression of the density-dependent gauge field $A_{\rm d}$ in equation (4). This approach treats the interaction effects to the zeroth order in perturbation, as we neglect the deviation in density profile from the single-particle eigenstates owing to interactions.

Analytically, we can obtain a qualitative understanding of the creation of the tilted double-well dispersion from perturbation theory. Performing the Jacobi–Anger expansion on the lattice potential, we arrive at

$$H = -\frac{\hbar^2}{2m}\partial_x^2 + \frac{U}{2}\cos k_0 x + H_1 = H_0 + H_1,$$

where H_0 describes the static lattice and H_1 describes the driving,

$$H_1 = \frac{U}{4} (e^{ik_0x} f + e^{-ik_0x} f^*),$$

$$f = -\frac{1}{4}(\alpha^2 + \beta^2) + 2i\alpha \sin \omega t - 2\alpha\beta \cos \omega t.$$

Here $\alpha = k_0 X_1$, $\beta = k_0 X_2$ and we keep terms up to the second order in α and β and up to ω in frequency.

The eigenstates of H_0 are the Bloch waves. Consider the states $|0,k\rangle$ and $|2,k\rangle$ in the ground and second excited bands at quasi-momentum k. Under rotating-wave approximation, the effective Hamiltonian is

$$H_{\rm eff} = \begin{pmatrix} E_0 & \Omega \\ \Omega^* & E_0 + \Delta \end{pmatrix},$$

where $E_0 = \langle 0, k | H_0 | 0, k \rangle$ is the energy of the ground band, Δ is the detuning and the coupling is

$$\Omega = \alpha \Omega_{-} - \alpha \beta \Omega_{+}.$$

Here $\Omega_{\pm} = \langle 0, k | \mathrm{e}^{\mathrm{i} k_0 x} \pm \mathrm{e}^{-\mathrm{i} k_0 x} | 2, k \rangle$ From here, we can see that the coupling has two contributions: one is the direct coupling $\Omega_1 = \alpha \Omega_-$ and the other is the Raman coupling $\Omega_2 = -\alpha \beta \Omega_+$. The parity of Ω_- is odd and that of Ω_+ is even, because the ground and second excited bands both have even-parity wavefunctions.

Near k=0, to the first order, the matrix elements depend on quasi-momentum k as $\Omega=\alpha\omega_0k-\alpha\beta\omega_1$, $E_0=\epsilon_0k^2$ and $\Delta=\epsilon_1k^2+\Delta_0$. Then the hybridized ground band dispersion is

$$E_{\rm g} = \epsilon_0 k^2 + \frac{1}{2} \left(\epsilon_1 k^2 + \Delta_0 - \sqrt{4(\alpha \omega_0 k - \alpha \beta \omega_1)^2 + \left(\epsilon_1 k^2 + \Delta_0 \right)^2} \right).$$

The dispersion has the shape of a double well because the coupling has a zero crossing near k=0. As the fundamental shaking frequency is red detuned, the coupling pushes down the ground-band energy. The tilt is a result of the constructive and destructive interference of Ω_1 and Ω_2 at positive and negative quasi-momentum, which pushes down the ground-band energy more on one side than the other. To the lowest order, this tilt is given by a linear term in the dispersion $2\alpha^2\beta\omega_0\omega_1k/\sqrt{4(\alpha\beta\omega_1)^2+\Delta_0^2}$, which effectively generates a static gauge field $A_s \simeq \beta = k_0 X_2$. The sign of the gauge field depends on the phase between the X_1 and X_2 lattice modulation components.

The numerical Floquet calculation indicates that the modulation weakly couples the ground band to the first excited band in addition to the second excited band. The coupling to the first excited band mostly contributes to a constant energy shift and does not qualitatively change the shape of the dispersion.

System preparation

In our experiment, the optical lattice is formed by a pair of counter-propagating 1,064-nm lasers, with lattice constant 532 nm. We use parameters lattice depth $U=8.9E_R$, where $E_R=h\times 1.3$ kHz is the recoil energy, and $\omega=2\pi\times 9,091$ Hz. Under our conditions, the factor η in equation (4) is $\eta=0.07m^*/\hbar k^*$, where $m^*=0.7m_0$ and $k^*=0.15k_1$.

After loading the atoms into the 1D optical lattice with harmonic confinement formed by 1,064-nm lasers, we prepare the BEC under a density-dependent gauge field by slowly ramping up the modulation amplitudes. We ramp up the amplitude X_1 to 7 nm over 11 ms (100 oscillation periods). As the critical shaking amplitude for the formation of double-well dispersion is 14 nm (obtained from the Floquet calculation of dispersion), the effective dispersion changes very little during this time, and we ramp quickly to reduce particle loss. We then ramp up the amplitude X_1 to 21 nm over another 289.3 ms (2,630 oscillation periods), which gives a ramp rate slow enough to suppress fluctuations from the Kibble–Zurek mechanism³⁰ and allow for deterministic evolution of the system. The amplitudes X_2 and a_{ac} are ramped to the final value over the first 11 ms. This ramp procedure turns on the gauge field slowly over time and results in a roughly constant critical density n_c throughout the ramp.

In Fig. 2h, the modulation amplitude at which the BEC momentum changes sign is estimated to be $14(2)a_{\rm B}$. To obtain this value, we fit the momentum-space distribution with two Gaussians and extract the population imbalance between the $\pm k^*$ states. We plot the imbalance against the modulation amplitude $a_{\rm ac}$ and fit with a hyperbolic tangent curve (see Extended Data Fig. 1). From the fitted position of the zero crossing, we obtain the value $14(2)a_{\rm B}$.

Although the dynamics during the ramp on of the gauge is deterministic, it is not quite adiabatic, as the two momentum minima are only offset by $h \times 3$ Hz, comparable with the ramp time 300 ms, and we do not arrive at the ground state. During the ramp fields, the cloud systematically shrinks, in part because of particle loss that reduces the chemical potential and in part because of the reduction of quantum pressure as the dispersion crosses the critical point from parabolic to double well, during which the effective mass diverges and the quantum pressure drops to zero. As we are in the Thomas–Fermi regime, the quantum

Article

pressure is usually negligible, but—in this case—its reduction is substantial enough to bias the domain formation because a slow ramp across the critical point is very susceptible to any bias. We have confirmed this effect in experiments with no gauge field (balanced double-well dispersion) and in numerical simulations without particle loss.

In Fig. 3e, we repeat the experiment at three different total particle numbers, 4.8×10^4 , 3.6×10^4 and 2.5×10^4 . The data shown in Fig. 3a–d are from the dataset with particle number 4.8×10^4 .

Extracting the domain densities from Bragg peaks

We extract the spatial distribution of the atoms in the $k=\pm k^*$ states following the technique in ref. 30 . At the time of detection, we switch off X_2 and $a_{\rm ac}$ and ramp the modulation amplitude X_1 to 140 nm over 0.8 ms. This pulse of lattice shaking excites the atoms from the ground band to superposition states of excited bands at the same quasi-momentum, which have oscillating projections to each Brillouin zone. Atoms in different quasi-momentum states have different oscillations. We image the atoms at the time when the projections of $k=\pm k^*$ states are maximally different. We perform a 6-ms time of flight to map the Brillouin zones to Bragg diffraction orders.

The densities in the Bragg diffraction orders

$$\mathbf{n}(x,y) = (n_{-1}(x,y), n_0(x,y), n_1(x,y))$$

is the sum of the contributions from atoms in the $k = \pm k^*$ states,

$$\mathbf{n} = n_{+}\hat{e}_{+} + n_{-}\hat{e}_{-}$$

where the basis vectors \hat{e}_{\pm} describe the distribution over the three Bragg diffraction orders of atoms in the $k=\pm k^*$ states. We calibrate the basis vectors \hat{e}_{\pm} by biasing the entire condensate into $k=\pm k^*$ and performing the same time-of-flight measurement. The basis vectors \hat{e}_{\pm} are L^1 normalized such that the components sum to 1. We determine the densities n_+ by fitting under the positivity constraint $n_+ > 0$.

The Bragg peaks of atoms in the $k = \pm k^*$ states are shifted relative to each other during the time of flight, because of the difference in quasi-momentum. We take this shift into account when reconstructing the domain densities. Additionally, this shift may cause originally disjoint domains to overlap during the time of flight. The coherent domains interfere in the overlapping region, forming density waves at wavenumber $2k^*$. This effect does not greatly alter the extracted domain structure or domain-wall position, and we neglect it in our analysis.

Analysis of the domain structures

Because we observe that the domain walls are mostly perpendicular to the lattice direction, in our analysis, we treat the domain structures as 1D. For the analysis in Fig. 3e, we integrate the mean and difference of the domain densities, $n = n_+ + n_-$ and $\Delta n = n_+ - n_-$, over the y direction and then select the central 10% of the cloud. Effectively, we select a central vertical strip of the cloud. We have checked that our results are not sensitive to the chosen strip width. From each experimental realization, we calculate the magnetization $M = \Delta n/n$ and we plot the average of n and M for each set of modulation amplitude $a_{\rm ac}$ and particle number N. We convert the 1D density to 3D density by dividing by the length scales in the y and z directions, l_y and l_z . As the chemical potential is not larger than the trap frequency in the z direction, we use the length scale of the harmonic oscillator ground state $l_z = \sqrt{h/m\omega}$. We obtain the length scale $l_y = \left(\int n \, \mathrm{d}y\right)^2/\int n^2 \, \mathrm{d}y$ from the measured density profiles n.

From the experiment data in Fig. 3e, we extract a value of $\epsilon_{\rm exp}$ in equation (5) by fitting to the expression

$$M = \tanh \frac{\ln n - \ln(\epsilon_{\rm exp}/g_{\rm ac})}{C},$$

with each data point in Fig. 3e corresponding to a magnetization M, a density n and a modulation strength $g_{\rm ac}$. This expression represents the relation $M={\rm sign}(n-\epsilon_{\rm exp}/g_{\rm ac})$, but smoothes the step function by a width parameter C. We present our fit to the experiment data in Extended Data Fig. 2.

For the analysis in Fig. 4c, we integrate the difference of the domain densities Δn over the y direction. We then extract the position of the zero crossing of the integrated 1D domain density by fitting a straight line to the six data points (each corresponding to a pixel in the image) around the numerical zero crossing, to improve accuracy. The error bars shown in Fig. 4c are 68% confidence intervals of this fit. With this procedure, we determine the domain-wall position with an uncertainty of around 0.3 microns.

We fit the domain-wall trajectories in Fig. 4c by assuming a common initial velocity for all ramp rates, a constant acceleration during the ramp that is independently varied for each ramp rate and a constant velocity after the ramp stops. The fitted initial velocity is $-17(10)~\mu m\, s^{-1},$ which we attribute to residual dynamics during the domain-formation process.

The conversion of the ramp rate \dot{a}_{ac} to the electric field $\mathcal E$ is derived from equation (4). We have

$$\mathcal{E} = \frac{4\pi\hbar^2}{m_0} n\eta \dot{a}_{ac},$$

with density $n = 2.8 \times 10^{13}$ cm⁻³ from the experiment. The prediction of parameter β for bare atoms is obtained from this relation and the charge-to-mass ratio $1/m^*$.

Data availability

The data that support the plots within this paper and other findings of this study are available from the corresponding author upon reasonable request. Source data are provided with this paper.

Code availability

The codes for the analysis of data shown within this paper are available from the corresponding author upon reasonable request.

Acknowledgements We thank E. Mueller for helpful discussions and K. Patel for carefully reading the manuscript. This work is supported by the National Science Foundation (NSF) grant no. PHY-2103542, NSF QLCI-HQAN no. 2016136, and the Army Research Office STIR grant W911NF2110108. Z.Z. is supported by the Grainger Graduate Fellowship.

Author contributions K.-X.Y. designed and performed the experiments and analysed the data. All authors contributed to discussions on the experiment and preparation of the manuscript. C.C. supervised the project.

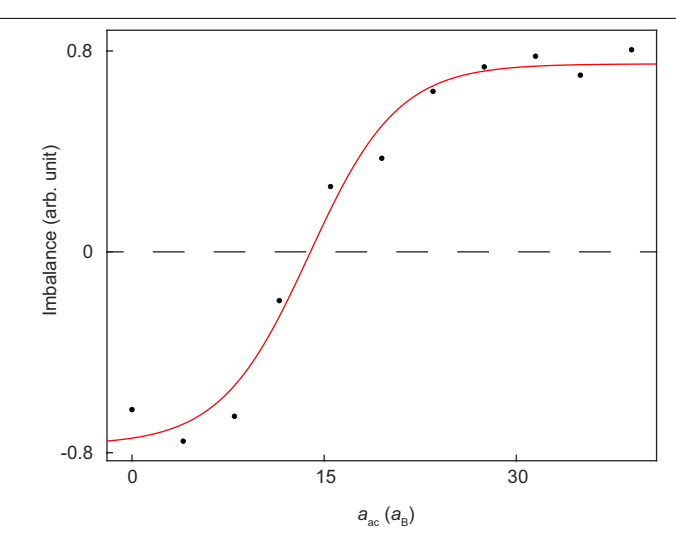
Competing interests The authors declare no competing financial interests.

Additional information

Supplementary information The online version contains supplementary material available at https://doi.org/10.1038/s41586-021-04250-3.

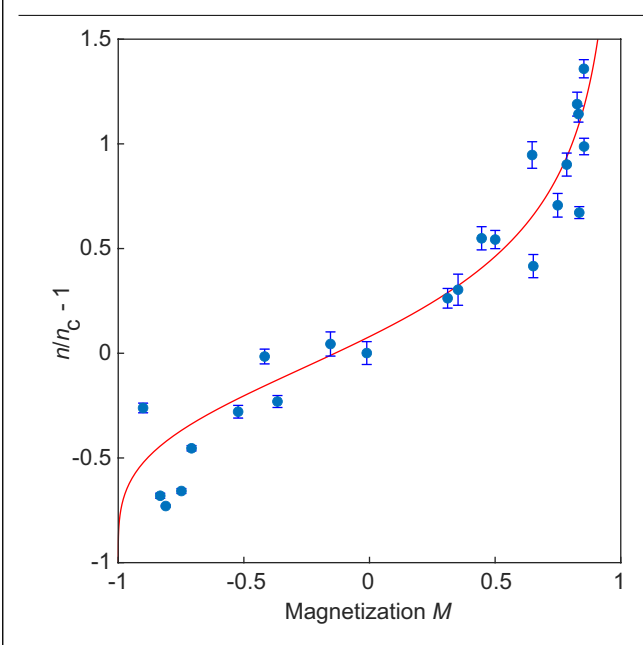
Correspondence and requests for materials should be addressed to Cheng Chin. Peer review information Nature thanks Pietro Massignan and the other, anonymous, reviewer for their contribution to the peer review of this work. Peer reviewer reports are available.

Reprints and permissions information is available at http://www.nature.com/reprints.



Extended Data Fig. 1|**Estimation of the zero-crossing position.** The population imbalance between the $\pm k^*$ states in Fig. 2h is fitted to extract the zero-crossing position.

Article



Extended Data Fig. 2 | **Extraction of** $\epsilon_{\rm exp}$ **from magnetization** *M***.** Experiment data in Fig. 3e are fitted to extract the value of $\epsilon_{\rm exp}$.